CHALMERS
UNIVERSITY OF TECHNOLOGY

Narrow-Line Width Emission and Room Temperature Amplified Spontaneous Emission in Three-Dimensional Ge Halide Perovskites

CHEMISTRY OF MATERIALS

pubs.acs.org/cm

Article

Narrow-Line Width Emission and Room Temperature Amplified Spontaneous Emission in Three-Dimensional Ge Halide Perovskites

Marta Morana,[▽] Andera Olivati,[▽] Marco Moroni, Giulia Folpini, Mehmet Baskurt, Margherita Garbaccio, Annamaria Petrozza, Francesco Ambrosio, Julia Wiktor, and Lorenzo Malavasi*

Cite This: *Chem. Mater.* 2026, 38, 6446−6455

Read Online

ACCESS | Metrics & More | Article Recommendations | Supporting Information

ABSTRACT: We report the structural and optoelectronic properties of lead-free $CsGeI_3$ and $CsGeBr_3$ perovskites, unveiling the critical role of local symmetry distortions in defining their emission properties. $CsGeBr_3$ exhibits broad photoluminescence from self-trapped excitons, due to local octahedral distortion and a large distribution of the average bond lengths. On the contrary, by using temperature-dependent pair distribution function analysis and hybrid-functional molecular dynamics simulations, we demonstrate that $CsGeI_3$ adopts a monoclinic local structure responsible for its narrow near-infrared (NIR) emission (~745 nm, FWHM ≈ 110 meV at room temperature), the narrowest reported for Ge-based perovskites and in line with tin iodide perovskites. Notably, the high level of structural order also supports the achievement of amplified spontaneous emission (ASE) at room temperature with an exceptionally low threshold (75 $\mu J/cm^2$), positioning it as a promising candidate for lead-free NIR light-emitting and laser applications.

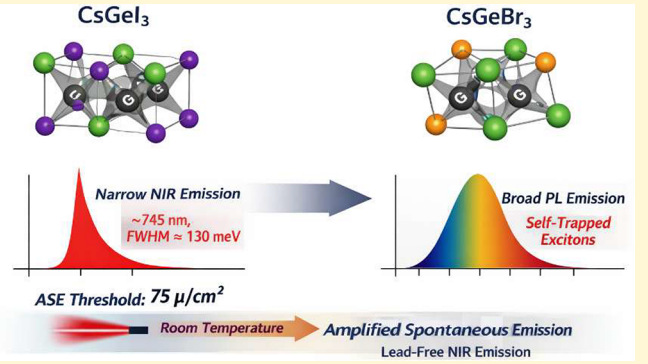

INTRODUCTION

Since they were first proposed as sensitizers for photovoltaic cells,[1] metal halide perovskites (MHPs) have attracted continuous interest thanks to their promising physical properties.[2−4] These compounds are described by the chemical formula ABX_3, where A is Cs or a small organic cation, B is a divalent metal cation, mostly lead, and X is a halide. The chemical composition strongly influences the crystalline and electronic band structures of MHPs, leading to a great variety in optoelectronic properties. Whereas many studies have focused on the role of different A-site cations and halide anions, the B-site cation, which most significantly affects the electronic structure of the semiconductor, has received less attention. Over the past decade, as an alternative to lead, tin halide perovskites have been the subject of intensive research, and more recently, attention has also turned to germanium-based perovskites.[5−12] The substitution of lead with tin leads to a narrowing of the semiconductor band gap, entering the near-infrared (NIR) spectral region by extending emission wavelengths to ~1000 nm, effectively covering the biological transparency window (650−950 nm) and the telecom window (800−900 nm). Near-infrared light-emitting sources have garnered significant interest for diverse applications, including night vision, biomedical treatments, optical communication, and data storage.[13,14] Currently, commercial sources utilize epitaxial heterostructures of III−V inorganic semiconductors as emitters, but, despite achieving nearly 100% internal quantum efficiency, they face limitations stemming from complex material processing and device architectures and, overall, the difficulty of integration in multicomponent photonic and electronic systems. Tin-halide perovskites have emerged as outstanding light-emitting materials due to their simple and versatile synthesis and exceptional optoelectronic properties. However, this class of perovskite still suffers from structural instability and poor control of the p-type self-doping, which leads to broad emission line width and nonradiative recombination of photo-carriers. Germanium halide perovskites share the same advantages of their tin counterparts, in particular, their great optoelectronic properties and the possibility of emission in the NIR region. In fact, germanium iodide-based perovskites show a photoluminescence peak in the spectral range from 650 to 800 nm.[14,15] Despite the good spectral range of operation of this class of materials, the Ge^{2+} cation has a smaller radius compared to lead and, for this reason, Ge-based perovskites often crystallize, at room temperature (RT), in a lower symmetry space group, usually *R*3*m* (No. 160), with respect to the *Pm*-3*m* (No. 221) of the

Received: February 9, 2026
Revised: June 17, 2026
Accepted: June 22, 2026
Published: July 3, 2026

perovskite aristotype.[16−18] Such an effect has been correlated to the expression of the ns^2 lone pair, more significant with a lower atomic number,[19−23] which becomes particularly evident in Ge-containing compounds where the off-centering of the B cation along the [111] direction induces significant distortions, leading to broad emission.[5,7] Such a close correlation between lone pair activity, structural distortion, and optoelectronic properties has been investigated, both at the average and local scales, for tin-based perovskites. For example, the local distortions generated by the activity of the lone pair in $FASnI_3$ [FA = formamidinium $[HC(NH_2)^{2+}]$ produce its typical broad energy distribution of the photoluminescence maximum.[24] On the other hand, despite the increasing interest in lead-free MHPs, detailed correlations of the average and local structure with the optoelectronic response are still lacking for the Ge-containing perovskites even if it is expected that the ease of distortion, due to the presence of the Ge^{2+} cation, may lead to a great tunability of the optical properties. For example, in the case of germanium iodide perovskites, unlike the lead and tin counterparts, changing the cation from Cs to methylammonium (MA) and to the bulkier acetamidinium leads to a large shift in the band gap of almost 1 eV (from 1.6 to 2.5 eV), while maintaining a rhombohedral perovskite structure.[17] A similar behavior is observed when changing the halogen atom from the larger iodide (I^-) to bromide (Br^-) and chloride (Cl^-), keeping the same cesium (Cs^+) cation. This halide compositional tuning results in band gap of 1.6, 2.3, and 3.4 eV, respectively,[25] which is also mirrored in an abundance of different emission peak positions and shapes.

To deepen the comprehension of the role of structural distortion on the optical properties of Ge-based perovskites, here we investigated the average and local structures and optical properties of $CsGeBr_3$ and $CsGeI_3$ as a function of temperature. The former shows a broad emission centered at 640 nm attributed to self-trapped exciton recombination, while the latter has a very narrow emission centered at 740 nm, making it a great candidate as an NIR emitter material. Moreover, $CsGeI_3$ perovskite crystallites show RT amplified spontaneous emission with a very low threshold (75 $\mu J/cm^2$), comparable to that of the much more studied LHP.

RESULTS AND DISCUSSION

Local Structure

$CsGeI_3$ and $CsGeBr_3$ polycrystalline samples have been synthesized according to the procedure reported in the Experimental Section in the Supporting Information (SI). RT laboratory X-ray diffraction confirms their single-phase nature (see Figure S1). In reciprocal space, temperature-dependent synchrotron X-ray diffraction data show that both $CsGeI_3$ and $CsGeBr_3$ crystallize in space group *R*3*m* in the whole temperature range investigated, in good agreement with previous literature reports (Figure S2). Moving into direct space and to the local scale, a visual inspection of the Pair Distribution Functions (PDFs) up to 5 Å from RT down to 90 K shows two peaks in the range of the Ge-X distances, consistent with a symmetry lower than cubic, such as the rhombohedral one (Figure 1).

Fitting of the RT PDF data of the iodide and bromide compounds in the *R*3*m* space group shows a relatively good agreement (see Figure 2a,c). It is worth noting that this space group was also proposed to describe the local structure of $FAPbBr_3$,[22] $MASnI_3$,[22,26] $FASnI_3$,[22,26] and several all-inorganic

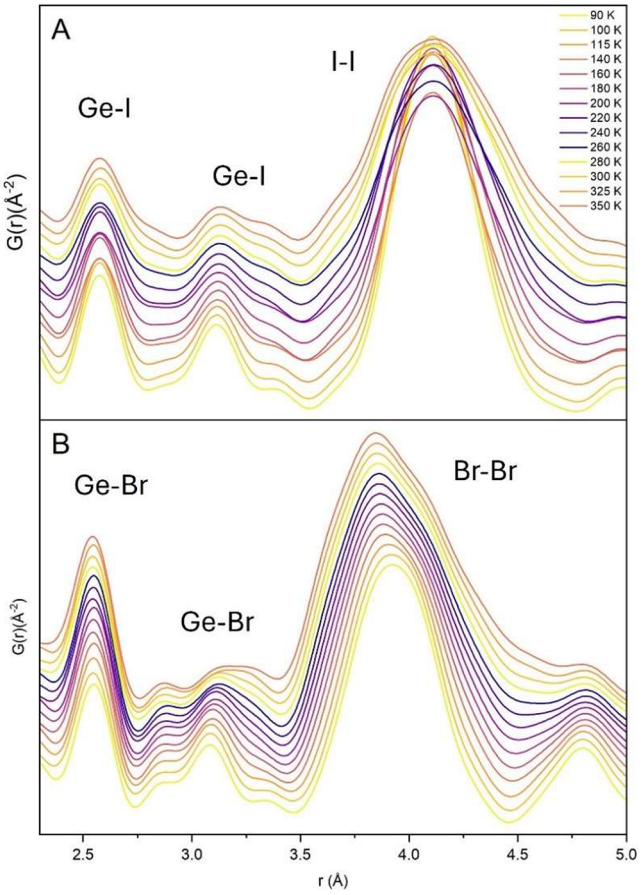

Figure 1. Overlay of the raw X-ray PDF data collected from 90 to 350 K for (A) $CsGeI_3$ and (B) $CsGeBr_3$.

titanates.[27−29] However, this symmetry does not allow for a good description of the shoulder visible on the second peak related to the Ge−X distances, more markedly in the iodide compound (Figure 2a, see arrow), suggesting that the symmetry at the local scale might be lower. Group-subgroup relationships identify space group *Cm* as a possible alternative. In space group *R*3*m*, the GeX_6 octahedra contain two groups of distances, whereas the lower monoclinic symmetry allows for four potential distributions of Ge−X bond lengths. A sketch of the rhombohedral and monoclinic unit cells is reported in Figure 2e,f, respectively.

As a matter of fact, the fitting of RT PDF data for $CsGeI_3$ against the monoclinic space group provides good agreement (see Figure 2b). Such symmetry properly describes the PDF data of $CsGeI_3$ also at low temperatures, as reported in Figure 3a.

On the other hand, at RT, $CsGeBr_3$ shows a less marked preference for the monoclinic symmetry, and fits against the *R*3*m* and *Cm* space groups provide similar agreement, with R_{wp} values of 15.0 and 15.6%, respectively (Figure 2c,d). *R*3*m* symmetry well describes the PDF of $CsGeBr_3$ even at 90 K (Figure 3b). It is important to note, however, that the bond-length distribution of the Ge−X octahedra appears to be broader for the $CsGeBr_3$ with respect to $CsGeI_3$, even though it is limited to two groups of bond lengths. This can be qualitatively assessed by looking at the second group of peaks in Figure 1. Notably, ab initio calculations showed that the root-mean-square-displacement (RMSD) of Ge in these compounds is greater for I than Br,[30] which could explain

https://doi.org/10.1021/acs.chemmater.6c00408
Chem. Mater. 2026, 38, 6446−6455

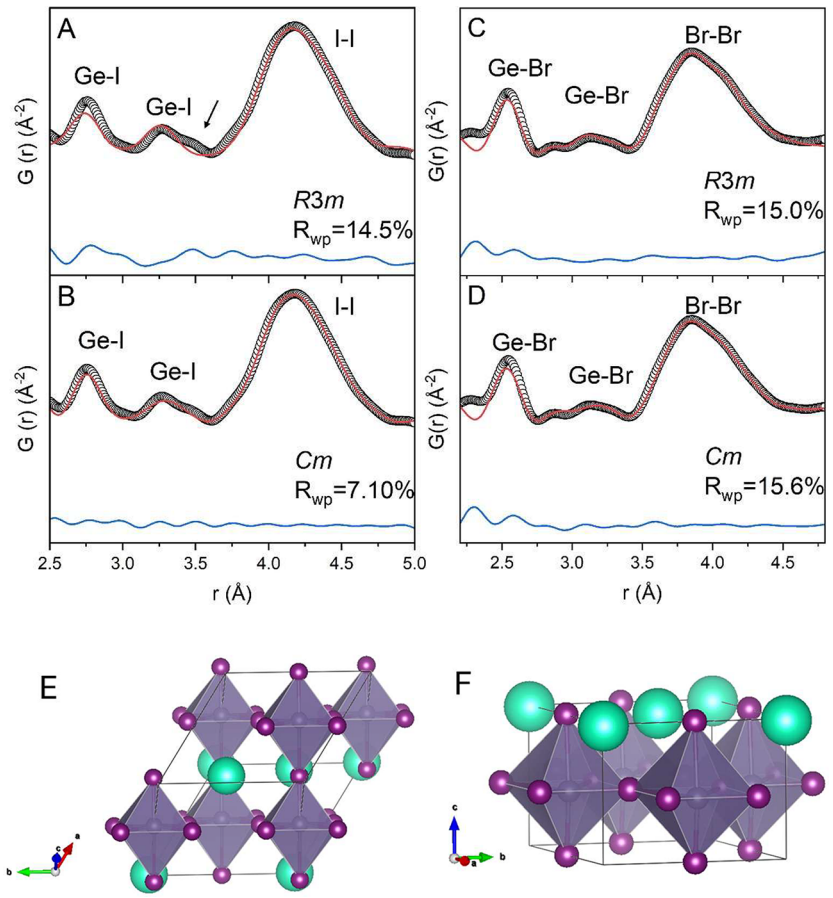

Figure 2. Fits of the RT X-ray PDF data for $CsGeX_3$ against space groups *R*3*m* and *Cm* for X = I (A, B) and X = Br (C, D). The arrow marks the shoulder on the second Ge−I distance described in the text. Sketches of the rhombohedral (E) and monoclinic (F) unit cells.

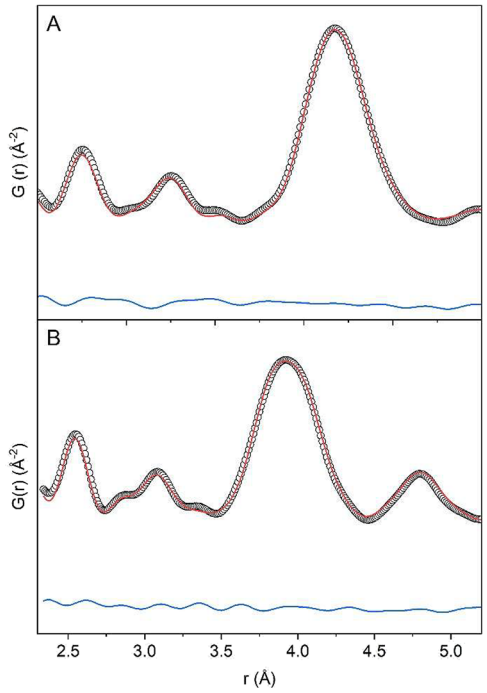

Figure 3. Fits of the X-ray PDF data for (A) $CsGeI_3$ against space groups *Cm* at 90 K (R_{wp} = 6.25%) and for (B) $CsGeBr_3$ against space groups *R*3*m* at 90 K (R_{wp} = 6.72%).

the slightly smaller distortion in the bromide MHPs. It appears that $CsGeX_3$ MHPs have a different general trend with respect to Pb and Sn compounds. In fact, these compounds usually adopt, at the local scale, a lower symmetry with respect to that of the average structures, whereas this tendency appears to be less significant for the Ge-containing counterparts. At lower temperatures, the data from $CsGeI_3$ cannot be fitted against the rhombohedral space group, but only against the monoclinic one (*Cm*) as shown in Figure 3a. This behavior is in good agreement with other MHPs that showed a trend of increasing distortion at the local scale upon cooling. It is worth noting that $FAGeBr_3$ was reported to crystallize in *Cm* at 100 K and that the local structure of several hybrid perovskites was reported to have the same symmetry as their low temperature average structure, namely $MAPbBr_3$,[31,32] $MAPbCl_3$,[33] $MASnBr_3$,[26] and $FASnBr_3$.[26] To complement the experimental total scattering results, we performed hybrid-functional molecular dynamics (MD) simulations at 100, 200, and 300 K for $CsGeI_3$ and $CsGeBr_3$. The simulated PDFs reproduce the experimental trend of temperature-induced broadening in the Ge−X and X−X correlations (Figure 4). A further comparison between the experimental and MD-calculated PDFs is reported in Figure S3. To this end, we selected 20 snapshots separated by 200 fs from each trajectory and calculated the average $G(r)$ plots for each material. The comparison between these average calculated PDFs and the experimental data at RT for the two compounds is given in Figure S3, where only the scale factor and the unit cell parameters have been refined. Overall, the calculated and experimental structures fairly agree in terms of

https://doi.org/10.1021/acs.chemmater.6c00408
Chem. Mater. 2026, 38, 6446−6455

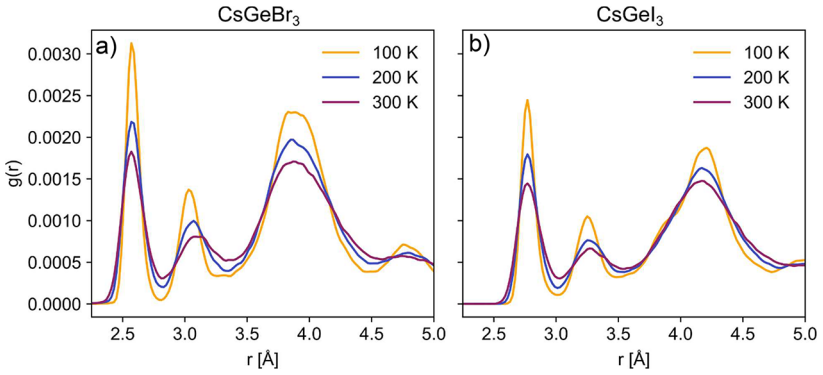

Figure 4. Calculated radial distribution functions from MD simulations for $CsGeX_3$, X = I, Br at 100, 200, and 300 K.

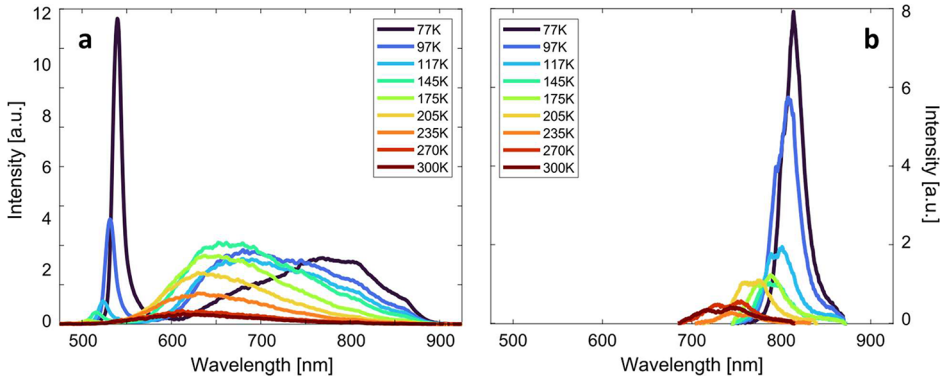

Figure 5. Photoluminescence spectra of (a) $CsGeBr_3$ and (b) $CsGeI_3$ powder samples as a function of temperature from RT to 77 K.

peak number, shape, and positions, supporting the validity of the computational modeling and strongly indicating that a proper description of the energy gaps in Ge halide perovskites requires the consideration of the local structural distortions experimentally unveiled by pair distribution function analysis. Such an approach allowed us to highlight the local symmetry characteristics of the two Ge perovskites, with the iodide sample described in the full temperature range with a monoclinic structure and the bromide sample showing a rhombohedral symmetry at 90 K and a monoclinic or rhombohedral symmetry at RT. Importantly, it appears that, the bond-length distribution of the $CsGeBr_3$ sample is broader than that of the iodide counterpart.

Although all structural and optical measurements were conducted under an inert atmosphere, the stability of the samples was systematically investigated in light of the well-known tendency of germanium-based perovskites to undergo oxidation and degradation under ambient conditions, driven by the oxidation of Ge^{2+}.[7] Laboratory powder XRD patterns have been collected on $CsGeI_3$ and $CsGeBr_3$ samples left open to the laboratory environment (about 20 °C and 30% relative humidity) as a function of time up to 336 h (Figure S4). Diffraction patterns are reported in Figure S4. It is interesting to note that $CsGeBr_3$ retains all of the peaks of the main phase up to the maximum time interval investigated, with the appearance of a few additional peaks (not directly corresponding to known oxidized phases). On the other hand, $CsGeI_3$ is significantly less stable, with a relevant decomposition of the perovskite phase occurring already after 48 h.

Optical Properties

Following the elucidation of the average and local structures of $CsGeI_3$ and $CsGeBr_3$ as a function of temperature, coupled with MD simulations, the optical properties of the two samples in powder form have been investigated by means of photoluminescence (PL) and absorption spectroscopies.

At RT, $CsGeBr_3$ has a band gap of 2.36 eV (525 nm) (see Figure S5) and shows a featureless and broad emission spectrum centered at 640 nm spanning through the entire visible range, with a full width at half-maximum (FWHM) of about 150 nm and a considerable Stokes shift (~100 nm). Such a kind of emission is usually ascribed to defect-mediated or self-trapped exciton recombination (STE). To further elucidate the origin of the optical properties of $CsGeBr_3$, we carried out low-T PL measurements as reported in Figure 5a. Upon decreasing the temperature down to 205 K, the emission intensity increases and the fwhm decreases, as expected. When reducing the density of phonons, some nonradiative pathways are hindered and the broadening of the emission peak is reduced. Further reducing the temperature down to 77 K, the peak position continues to linearly redshift but changes its slope, on the contrary the FWHM increases (Figure S6). This observation is in accordance with the PDF results reported above, highlighting a potential difference between the distortion degree at RT and at cryogenic temperatures. Additional evidence for this structural change is provided by the sample color change from ocher at RT to dark red at 77 K, as shown in the inset in Figure S6. Moreover, at 175 K, a narrow peak (FWHM ~ 13 nm) related to excitonic recombination emerges and becomes the dominant emission at 77 K.

To identify the nature of the broad emission in $CsGeBr_3$, we performed excited-state calculations which found a stable self-trapped exciton (STE) with a formation energy of −0.41 eV in the material (see Figure 6), consistent with the STE stability

https://doi.org/10.1021/acs.chemmater.6c00408
Chem. Mater. 2026, 38, 6446−6455

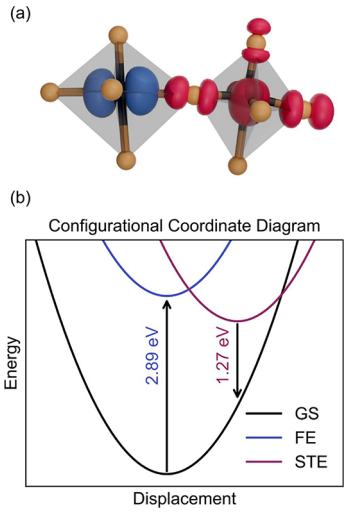

Figure 6. (a) Self-trapped exciton (STE) configuration in $CsGeBr_3$ from hybrid-DFT excited-state calculations, showing electron (blue) and hole (red) localization on neighboring Ge-centered octahedra and the associated local lattice relaxation. (b) Configurational-coordinate diagram illustrating vertical absorption and emission energies; the emission energy is estimated from the singlet−triplet total-energy difference evaluated at the relaxed STE geometry.

previously reported for $CsGeBr_3$ using hybrid density functional theory.[34] The STE corresponds to the localization of the electron and hole on neighboring Ge-centered octahedra. This localization induces a strong local lattice relaxation, with Ge−Br bonds elongating around the electron-trapping site and contracting around the hole-trapping site. Such a displaced excited-state minimum naturally leads to a large Stokes shift and broad emission, as radiative recombination occurs from a strongly relaxed geometry and is therefore accompanied by significant vibronic broadening. Using the relaxed STE geometry, we estimate the emission energy from the total-energy difference between the triplet and singlet states evaluated at the STE geometry (see SI for details).

Changing the anion from bromine to iodine greatly alters the emission properties (see Figure 5b). At RT, the emission, centered at 745 nm, is characterized by a narrow peak (FWHM ∼ 70 nm/130 meV) with a minimal Stokes shift (band gap = 1.61 eV/740 nm, Figure S5). The double peak that characterizes the shape of the emission is caused by the self-absorption and multiple reflections of emitted photons in the powder samples.[35] This is further corroborated by the identical lifetime of the two peaks extracted by time-resolved photoluminescence measurements (TRPL) as observed in Figure S7. Lowering the temperature, the FWHM monotonically decreases to less than 30 nm (50 meV) at 77 K (Figure S8), consistent with the above-reported total scattering data, which indicate that the local monoclinic structure actually describes the octahedral distortion in the whole temperature range. We emphasize that the emission width is the lowest for any germanium-based perovskite both at RT (∼140 meV) and 77 K (∼50 meV). These values are comparable with optimized thin films or single crystals of $CsPbI_3$ and lower than those of the tin counterpart, making $CsGeI_3$ perovskite a great candidate for light-emitting applications.[12,36]

We note that in $CsGeI_3$, the formation of STEs, obtained with excited-state calculations, is not favorable, explaining the lack of Stokes shift in this material and the comparatively narrow emission observed experimentally. This indicates that photoexcited carriers in $CsGeI_3$ remain mainly in near-band-edge states rather than relaxing into strongly distorted self-trapped configurations. This is favorable for achieving optical gain since STE formation would act as a loss channel by localizing carriers and broadening the emission spectrum. In contrast, $CsGeBr_3$ hosts a stabilized STE minimum, and using the relaxed STE geometry, we estimate an emission energy of 1.27 eV at 0 K (see Figure 6). This value is lower than the emission energy extrapolated from the experimental spectra to 0 K (≈1.55 eV), which can be rationalized by the approximate nature of the computational estimate: the calculated value corresponds to a vertical singlet−triplet energy difference evaluated at the triplet geometry and therefore neglects nuclear quantum effects (zero-point motion) and finite-temperature dynamic disorder contributions that are expected to renormalize the excited-state potential energy surfaces. In addition, small systematic errors associated with the electronic-structure description of localized excited states (e.g., exchange−correlation functional dependence) can contribute to residual offsets. Despite this quantitative difference, the calculations capture the key qualitative trend, namely that STE formation is energetically favored in $CsGeBr_3$ but suppressed in $CsGeI_3$, providing a rationale for the broad, strongly Stokes-shifted

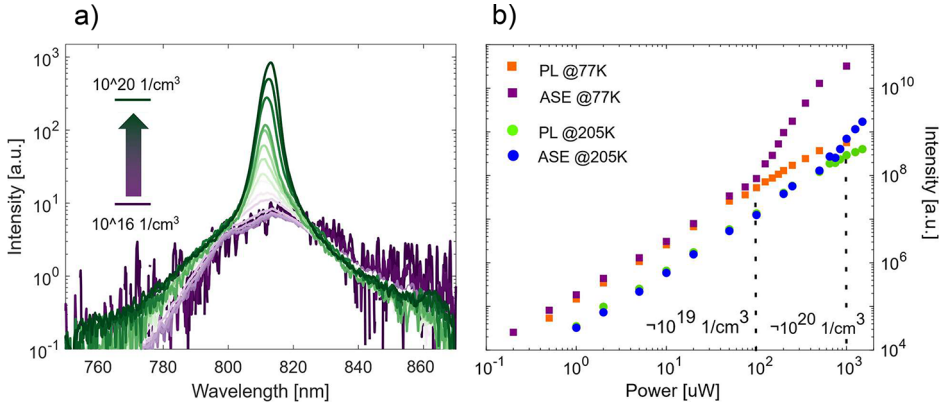

Figure 7. (a) PL spectra of $CsGeI_3$ sample taken at 77 K for different laser fluences from 10^{16} to 10^{20} photons/cm^3 and (b) power dependent emission intensity for the narrow (ASE) and broad (PL) peak at different temperatures: 77 K (violet and orange and green) and 205 K (blue and green).

https://doi.org/10.1021/acs.chemmater.6c00408
Chem. Mater. 2026, 38, 6446−6455

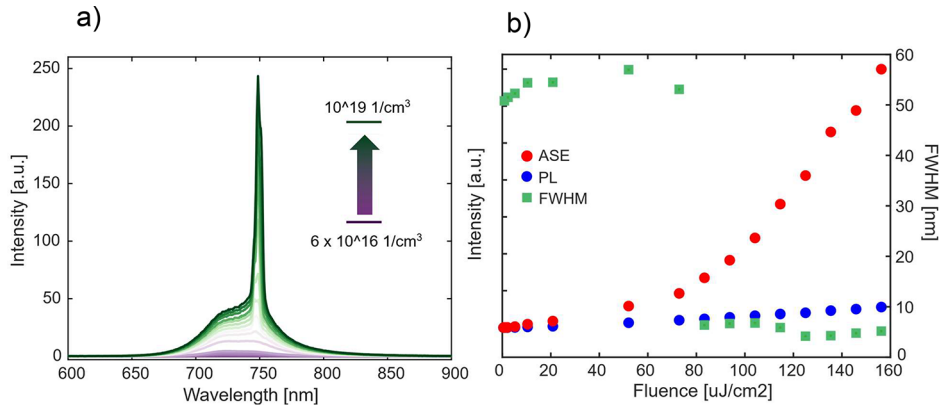

Figure 8. (a) Fluence dependent PL spectra of $CsGeI_3$ crystallites at room temperature. (b) Fluence dependent emission intensity for the narrow (ASE, red dot), broad (PL blue dot), and fwhm (green square) of the dominant emission.

emission of the bromide and the narrow, near-band-edge emission of the iodide observed in experiments.

The temperature evolution of the band gap was also extracted from the MD simulations and follows the experimental trend (Figure S9), with $CsGeBr_3$ showing a stronger blueshift with an increase in temperature. This trend can be seen also by monitoring the emission position of the two samples in the same temperature range analyzed: in the case of $CsGeBr_3$ perovskite, we can see a shift of the broad peak of about 250 meV, while for the $CsGeI_3$ sample the shift is reduced to 150 meV (see Figure 5). The lower shift of the band gap upon lowering the temperature, in addition to the very narrow emission, suggests a low amount of defects and a low coupling with phonons.

To further investigate the optical properties of $CsGeBr_3$ and $CsGeI_3$, we performed fluence-dependent measurements at different temperatures in a fluence range from 10^{16} to 10^{20} absorbed photons/cm^3. To address the origin of the emission of the bromine sample, we fit the fluence dependence of the two emission peaks with a power law, $I = P^K$, as shown in Figure S10. Fitting the measurement taken at 97 K as a reference, we obtained values of 1.005 and 0.7915 for the narrow and broad emissions, respectively. A value of the exponential K close to 1 suggests excitonic recombination, while a lower value is related to defect-mediated recombination or self-trapped excitons. This, in addition to the lattice distortion due to Ge substitution and the above-reported excited-state calculations, corroborates the idea of excitonic and defect-mediated/STE recombination for the narrow and broad emissions from $CsGeBr_3$, respectively.[37,38]

The $CsGeI_3$ sample, in the temperature range from 300 to 235 K, shows a superlinear behavior vs fluence, suggesting a gain process in the material (Figure S11). As shown in Figure 7a, by further lowering the temperature, a narrow peak (FWHM 4−8 nm) starts to appear at 77 K, centered at 815 nm. As can be seen from Figure 7b, its intensity rises exponentially with the incident fluence, suggesting an amplified spontaneous emission (ASE) process.

Figure 7b shows the comparison of the intensity of the broad emission and the narrow ASE peak vs incident light power at 205 and 77 K. The point from which the ASE peak starts to have an exponential trend is the threshold for ASE. As we can notice, the threshold decreases from 10^{20} (4300 μJ/cm^2) to 10^{19} (430 μJ/cm^2) upon lowering the temperature down to 77 K. We stress the fact that these results were obtained by measuring powder samples, in which the problem of reabsorption and a huge amount of scattering usually make it really difficult to achieve ASE.[39]

Driven by these encouraging results, we moved to deposit $CsGeI_3$ on a glass substrate through a one-step deposition (see SI). The crystal structure is confirmed by XRD measurements (Figure S12), with the main peaks corresponding to the calculated average rhombohedral structure $R3m$ as reported above. Scanning electron microscopy (SEM) images (Figure S13) show that $CsGeI_3$ does not cover the substrate uniformly, but the sample is composed of large crystalline islands of perovskite measuring tens of μm, together with smaller grains. Having proven the right composition and structure, we performed absorption and fluence dependence PL measurements at RT over a fluence range of more than 2 orders of magnitude.

The absorption edge of the $CsGeI_3$ crystallites deposited on glass is comparable to that of the powder sample, 1.64 eV, as shown in Figure S14. Moreover, looking at the emission spectra shape (Figure S15), we can notice that the emission of the perovskite crystallites overlaps with that of the powder sample and that the second peak intensity is greatly reduced, as expected, due to the decreased reabsorption and scattering, revealing a FWHM of 110 meV (~50 nm). As we can observe from Figure 8a, by increasing the fluence on the sample, a narrow ASE peak appears at 748 nm. From the trend of the FWHM and peak intensity at 748 nm by increasing the incident fluence, it is possible to extrapolate the threshold of this phenomenon. At the threshold of ASE, the FWHM of the dominant emission decreases from more than 30 nm to 4−6 nm and the intensity at 748 nm (red dot in Figure 8b) starts rising exponentially, while the broad peak (blue dots) follows a linear trend. The value at which this occurs is around 75 μJ/cm^2, which is an incredibly low value for a novel material, even compared to the lead and tin counterparts, whose threshold usually lie in a range between 0.5 and hundreds of μJ/cm^2 for optimized deposition, passivation, and measurement conditions.[40] To the best of our knowledge, this is the first reported measured ASE in a fully inorganic germanium perovskite. Further investigations on the deposition method are needed in order to obtain a uniform layer of perovskite, thereby reducing roughness and defectivity.

Taken together, our structural, computational, and optical results show that emission in $CsGeX_3$ is governed not by average crystallographic symmetry alone, but by the topology

https://doi.org/10.1021/acs.chemmater.6c00408
Chem. Mater. 2026, 38, 6446−6455

of the local distortion landscape created by the Ge^{2+} off-centering. In $CsGeI_3$, PDF analysis and hybrid-functional MD reveal a coherent symmetry lowering to a monoclinic local motif that persists over the investigated temperature range and is associated with a comparatively narrow Ge−I bond-length distribution. Thus, the lone-pair-driven distortion is accommodated within a single local geometry, so that photoexcitation requires only limited further lattice reorganization. Consistent with the minimal Stokes shift, the smaller temperature-induced spectral renormalization, and the absence of a favorable self-trapped exciton minimum in the excited-state calculations, the emissive state remains predominantly near-band-edge and only weakly coupled to the lattice, thereby enabling narrow line widths and optical gain. By contrast, $CsGeBr_3$ exhibits a broader Ge−Br bond-length distribution despite its nominally higher local symmetry. In this case, the excited state couples more strongly to lattice distortions and relaxes into a localized self-trapped exciton, yielding the large Stokes shift and STE-like fluence dependence observed experimentally. The key design rule that emerges is that narrow-band lead-free perovskite emitters should be sought among compositions that enforce a single, well-defined local distortion with low bond-length variance and no stabilized self-trapped excited-state minimum, whereas broad emitters will arise when symmetry breaking is spatially distributed and accompanied by strong excited-state lattice relaxation. This predicts that the best narrow-band candidates will combine narrow PDF/MD bond-length histograms, weak temperature-dependent line width or band-edge renormalization, and the absence of persistent carrier localization in excited-state calculations.

CONCLUSIONS

In this work, we have explored the structural and optical properties of the lead-free germanium halide perovskites $CsGeI_3$ and $CsGeBr_3$. Both compounds crystallize in the rhombohedral space group $R3m$, but total scattering and PDF analysis indicate a lower symmetry at the local scale, capable of describing the observed broad distribution in the Ge−X bond lengths. While for $CsGeI_3$ a monoclinic structure well describes the local structure in the whole temperature range, in the case of $CsGeBr_3$ a possible variation of the local structure has been found from RT to low temperatures, coupled to a broader Ge−X bond distribution. The analysis of the optical response shows that $CsGeBr_3$ exhibits broad, featureless photoluminescence centered at 640 nm with a large Stokes shift (∼100 nm) and a FWHM of 150 nm, indicative of defect-mediated or STE recombination. Excited-state calculations confirm the presence of a stable STE with a formation energy of −0.41 eV, and fluence-dependent measurements show a sublinear power-law exponent ($K \approx 0.79$), further supporting this recombination mechanism. Upon cooling, $CsGeBr_3$ we can see the emergence of a sharp excitonic peak (FWHM ∼ 13 nm) and a shrinkage followed by a broadening of the main emission peak in accordance to the preferences of the local symmetry extrapolated from PDF data. In contrast, $CsGeI_3$ displays a notably different behavior. At RT, the emission consists of a narrow peak centered at 745 nm with a minimal Stokes shift and a FWHM of ∼110 meV, narrowing to ∼50 meV at 77 K. This emission is the narrowest reported for germanium-based perovskites and rivals that of optimized lead and tin halide perovskites thin films, making this material a promising option for LED applications. Fluence-dependent measurements reveal superlinear behavior in the 300−235 K range, suggesting a gain process and, at 77 K, a narrow ASE peak emerges at 815 nm. The ASE threshold decreases significantly with temperature, from 4300 to 430 $\mu J/cm^2$. Remarkably, $CsGeI_3$ crystallites deposited on glass via a one-step deposition exhibit ASE at 748 nm with a low threshold (75 $\mu J/cm^2$), which is among the lowest reported for lead-free perovskites. This achievement is particularly notable, making this material a great candidate as a gain material for laser applications.

EXPERIMENTAL SECTION

Synthesis

$CsGeI_3$ and $CsGeBr_3$ powdered samples were prepared starting from stoichiometric amounts of germanium bromide or iodide and cesium bromide or iodide dissolved in excess HBr or HI, respectively. After heating to 90 °C while stirring, the solution was then heated to 100 °C for 30 min and left to cool at 1 °C/min. $CsGeI_3$ deposited on glass/ITO substrates were produced with a one-pot approach. We dissolved 80 μg of CsI and 100 μg of GeI_2 in 2 mL of DMF, then stirred and heated the solution at 120 °C for 1 h. 20 μL of the solution, after being filtered, was deposited on plasma-treated grass or ITO substrates. As the last step, the samples were placed on a hot plate at 60 °C for 5 min for a fast annealing process. Samples quality was checked by laboratory XRD using a Bruker D6 Cu-anode diffractometer.

X-ray Total Scattering

X-ray PDF data were collected at the ID11 materials science beamline at ESRF, Grenoble, (λ = 0.158135 Å), using a FReLoN camera. The sample-to-detector distance (105 mm) was calibrated against a CeO_2 standard using the pyFAI[41] package, which was also employed to integrate the 2D images. Sample powders were loaded into quartz capillaries (provided by Hilgenberg) with a 0.5 mm diameter, which were spun during data collection. A Cryostream was employed to collect low- and high- temperature data from 80 to 360 K. PDFs were obtained using PDFgetX3[42] with a Q_{max} of 26 Å and PDF modeling was carried out using PDFGui.[43] The instrumental parameters Q_{broad} and Q_{damp} were set to 0 and 0.046, respectively, as determined from the CeO_2 standard. Starting coordinates for the various structural models were obtained from literature data and from calculations in ISODISTORT,[44,45] starting from the reported model and employing "method 1" in the search.

Optical Measurements

Static and time-resolved photoluminescence measurements were performed by exciting the sample with the third harmonic (355 nm) of a Nd:YAG Picolo-AOT laser (pulse length of 1000 ps, 1 kHz repetition rate). The laser was focused on the sample placed in a cooled Linkam stage under vacuum. The emission of the samples was collected with an Andor iStar 320T ICCD camera coupled to a Shamrock 303i spectrograph.

Absorption measurements on $CsGeI_3$ deposited on a glass substrate were performed using a UV−vis spectrometer (PerkinElmer Lambda 1050).

Crystallites Characterization

XRD measurements on $CsGeI_3$ deposited on a glass substrates were performed using a BrukerTM diffractometer equipped with a CuK anode (λ = 1.544060 Å). The samples were kept in a controlled nitrogen environment to prevent degradation. SEM images were acquired with a MIRA3 TESCAN system with an accelerating voltage of 5 kV.

COMPUTATIONAL DETAILS

Ab initio molecular dynamics (MD) simulations were carried out for $CsGeBr_3$ and $CsGeI_3$ using the CP2K package within the Quickstep module.[46,47] A hybrid exchange-correlation functional (PBE0-TC-LRC) was used, with the fraction of

https://doi.org/10.1021/acs.chemmater.6c00408
Chem. Mater. 2026, 38, 6446−6455

exact exchange, α determined via the Koopmans' condition in ref 8: 26% for $CsGeBr_3$ and 21% for $CsGeI_3$.[48] The auxiliary density matrix method (ADMM) was employed together with the truncated Coulomb operator (6 Å cutoff), using Goedecker–Teter–Hutter pseudopotentials and MOLOPT basis sets. Simulations were run in the NVT ensemble at 100, 200, and 300 K, using volumes matched to experimental unit cells at each temperature. A Nosé thermostat was applied. Each trajectory consisted of 7–8 ps, with the first 1.5 ps discarded for equilibration. The time step was 5 fs. The average band gap at each temperature was computed from instantaneous HOMO–LUMO gaps sampled every 0.5 ps. Spin–orbit coupling (SOC) corrections to the band gap were calculated using VASP by comparing calculations with and without SOC.[49,50]

To investigate the nature of the broad emission in $CsGeBr_3$, we performed excited-state calculations on a monoclinic supercell in the triplet state. The STE was localized by relaxing the triplet state at 0 K with initial distortions around neighboring Ge atoms. The STE localization protocol follows ref 11. The STE formation energy (E_f^{STE}) was computed as the adiabatic stabilization of the localized triplet configuration relative to the delocalized excitation:

$$E_f^{STE} = E_T^{STE} - E_S^{GS} - E_{gap}$$

where E_T^{STE} is the total energy of the relaxed triplet STE configuration, E_S^{GS} is the total energy of the relaxed singlet ground state, and E_{gap} is the band gap computed with the same hybrid functional and exact-exchange fraction α (estimated from the Kohn–Sham HOMO–LUMO gap). The emission energy was estimated using a ΔSCF approach as the vertical singlet–triplet energy difference evaluated at the relaxed STE geometry.

■ ASSOCIATED CONTENT

Supporting Information

The Supporting Information is available free of charge at https://pubs.acs.org/doi/10.1021/acs.chemmater.6c00408.

Experimental and computational methods; additional experimental data (PDF)

■ AUTHOR INFORMATION

Corresponding Author

Lorenzo Malavasi − *Department of Chemistry and INSTM, University of Pavia, 27100 Pavia, Italy;* orcid.org/0000-0003-4724-2376; Email: lorenzo.malavasi@unipv.it

Authors

Marta Morana − *Department of Earth Sciences, University of Firenze, 5012 Firenze, Italy;* orcid.org/0000-0002-5724-9216

Andera Olivati − *Center for Nano Science and Technology, Istituto Italiano di Tecnologia, 20134 Milano, Italy;* orcid.org/0009-0003-7285-3141

Marco Moroni − *Department of Chemistry and INSTM, University of Pavia, 27100 Pavia, Italy;* orcid.org/0000-0001-6167-3792

Giulia Folpini − *Institute for Photonics and Nanotechnology, CNR − IFN, 20133 Milano, Italy; Center for Nano Science and Technology, Istituto Italiano di Tecnologia, 20134 Milano, Italy*

Mehmet Baskurt − *Department of Physics and Astronomy, Chalmers University of Technology, 41296 Gothenburg, Sweden;* orcid.org/0000-0001-7181-6814

Margherita Garbaccio − *Department of Chemistry and INSTM, University of Pavia, 27100 Pavia, Italy*

Annamaria Petrozza − *Center for Nano Science and Technology, Istituto Italiano di Tecnologia, 20134 Milano, Italy;* orcid.org/0000-0001-6914-4537

Francesco Ambrosio − *Dipartimento di Scienze di Base e Applicate (DiSBA), Università degli Studi della Basilicata, 85100 Potenza, Italy;* orcid.org/0000-0002-6388-9586

Julia Wiktor − *Department of Physics and Astronomy, Chalmers University of Technology, 41296 Gothenburg, Sweden;* orcid.org/0000-0003-3395-1104

Complete contact information is available at: https://pubs.acs.org/10.1021/acs.chemmater.6c00408

Author Contributions

[▽]M.M. and A.O. equally contributed to the paper.

Notes

The authors declare no competing financial interest.

■ ACKNOWLEDGMENTS

L.M. acknowledges support from the Ministero dell'Università e della Ricerca (MUR) and the University of Pavia through the program "Dipartimenti di Eccellenza 2023–2027". We acknowledge support from the Italian Ministry of Research under the PRIN 2022 Grant No 2022F2K7J5 with the title "Two-dimensional chiral hybrid organic–inorganic perovskites for chiroptoelectronics" PE 3 funded by PNRR Mission 4 Istruzione e Ricerca - Component C2 - Investimento 1.1, Fondo per il Programma Nazionale di Ricerca e Progetti di Rilevante Interesse Nazionale PRIN 2022 - CUP B53D23004130006. L.M. and M.M. acknowledge the Fondazione Cariplo through the program "Young Researchers", Grant No. 2023-1246. F.A. gratefully acknowledges 2022-PNRR grant (P2022W9773). M.B. and J.W. acknowledge support from the Swedish Strategic Research Foundation through a Future Research Leader programme (FFL21-0129), the European Research Council (ERC Starting Grant No. 101162195), and the Knut and Alice Wallenberg Foundation (No. 2023.0032). The computations were enabled by resources provided by the National Academic Infrastructure for Supercomputing in Sweden (NAISS), partially funded by the Swedish Research Council through grant agreement no. 2022-06725.

■ REFERENCES

(1) Kojima, A.; Teshima, K.; Shirai, Y.; Miyasaka, T. Organometal Halide Perovskites as Visible-Light Sensitizers for Photovoltaic Cells. *J. Am. Chem. Soc.* **2009**, *131* (17), 6050–6051.

(2) Brenner, T. M.; Egger, D. A.; Kronik, L.; Hodes, G.; Cahen, D. Hybrid Organic—Inorganic Perovskites: Low-Cost Semiconductors with Intriguing Charge-Transport Properties. *Nat. Rev. Mater.* **2016**, *1* (1), 1–16.

(3) Meggiolaro, D.; Ambrosio, F.; Mosconi, E.; Mahata, A.; De Angelis, F. Polarons in Metal Halide Perovskites. *Adv. Energy Mater.* **2020**, *10* (13), 1902748.

(4) Romani, L.; Malavasi, L. Solar-Driven Hydrogen Generation by Metal Halide Perovskites: Materials, Approaches, and Mechanistic View. *ACS Omega* **2020**, *5* (40), 25511–25519.

(5) Chiara, R.; Accorsi, G.; Listorti, A.; Coduri, M.; Coccia, C.; Tedesco, C.; Morana, M.; Malavasi, L. Halide Alloying and Role of

Central Atom on the Structural and Optical Properties of Decylammonium Germanium 2D Perovskites. *APL Energy* **2023**, *1* (1), No. 016101.
(6) Romani, L.; Speltini, A.; Chiara, R.; Morana, M.; Coccia, C.; Tedesco, C.; Armenise, V.; Colella, S.; Milella, A.; Listorti, A.; Profumo, A.; Ambrosio, F.; Mosconi, E.; Pau, R.; Pitzalis, F.; Simbula, A.; Ricciarelli, D.; Saba, M.; Medina-Llamas, M.; De Angelis, F.; Malavasi, L. Air- and Water-Stable and Photocatalytically Active Germanium-Based 2D Perovskites by Organic Spacer Engineering. *Cell Reports Physical Science* **2023**, *4* (1), No. 101214.
(7) Chiara, R.; Morana, M.; Malavasi, L. Germanium-Based Halide Perovskites: Materials, Properties, and Applications. *ChemPlusChem.* **2021**, *86* (6), 879−888.
(8) Ray, D.; Clark, C.; Pham, H. Q.; Borycz, J.; Holmes, R. J.; Aydil, E. S.; Gagliardi, L. Computational Study of Structural and Electronic Properties of Lead-Free CsMI3 Perovskites (M = Ge, Sn, Pb, Mg, Ca, Sr, and Ba). *J. Phys. Chem. C* **2018**, *122* (14), 7838−7848.
(9) Bhaumik, S.; Ray, S.; Batabyal, S. K. Recent Advances of Lead-Free Metal Halide Perovskite Single Crystals and Nanocrystals: Synthesis, Crystal Structure, Optical Properties, and Their Diverse Applications. *Materials Today Chemistry* **2020**, *18*, No. 100363.
(10) De Angelis, F. The Prospect of Lead-Free Perovskite Photovoltaics. *ACS Energy Lett.* **2021**, *6* (4), 1586−1587.
(11) Dong, H.; Ran, C.; Gao, W.; Li, M.; Xia, Y.; Huang, W. Metal Halide Perovskite for Next-Generation Optoelectronics: Progresses and Prospects. *eLight* **2023**, *3* (1), 3.
(12) Pitaro, M.; Tekelenburg, E. K.; Shao, S.; Loi, M. A. Tin Halide Perovskites: From Fundamental Properties to Solar Cells. *Adv. Mater.* **2022**, *34* (1), 2105844.
(13) Xu, M.; Li, X.; Liu, S.; Zhang, L.; Xie, W. Near-Infrared Organic Light-Emitting Materials, Devices and Applications. *Mater. Chem. Front.* **2023**, *7* (20), 4744−4767.
(14) Liu, Y.; Di Stasio, F.; Bi, C.; Zhang, J.; Xia, Z.; Shi, Z.; Manna, L. Near-Infrared Light Emitting Metal Halides: Materials, Mechanisms, and Applications. *Adv. Mater.* **2024**, *36* (21), 2312482.
(15) Lü, X.; Stoumpos, C.; Hu, Q.; Ma, X.; Zhang, D.; Guo, S.; Hoffman, J.; Bu, K.; Guo, X.; Wang, Y.; Ji, C.; Chen, H.; Xu, H.; Jia, Q.; Yang, W.; Kanatzidis, M. G.; Mao, H.-K. Regulating Off-Centering Distortion Maximizes Photoluminescence in Halide Perovskites. *National Science Review* **2021**, *8* (9), nwaa288.
(16) Thiele, G.; Rotter, H. W.; Schmidt, K. D. Kristallstrukturen und Phasentransformationen von Caesiumtrihalogenogermanaten(II) CsGeX3 (X = Cl, Br, I). *Z. Anorg. Allg. Chem.* **1987**, *545* (2), 148−156.
(17) Stoumpos, C. C.; Frazer, L.; Clark, D. J.; Kim, Y. S.; Rhim, S. H.; Freeman, A. J.; Ketterson, J. B.; Jang, J. I.; Kanatzidis, M. G. Hybrid Germanium Iodide Perovskite Semiconductors: Active Lone Pairs, Structural Distortions, Direct and Indirect Energy Gaps, and Strong Nonlinear Optical Properties. *J. Am. Chem. Soc.* **2015**, *137* (21), 6804−6819.
(18) Liu, Y.; Gong, Y.-P.; Geng, S.; Feng, M.-L.; Manidaki, D.; Deng, Z.; Stoumpos, C. C.; Canepa, P.; Xiao, Z.; Zhang, W.-X.; Mao, L. Hybrid Germanium Bromide Perovskites with Tunable Second Harmonic Generation. *Angew. Chem., Int. Ed.* **2022**, *61* (43), No. e202208875.
(19) Fabini, D. H.; Laurita, G.; Bechtel, J. S.; Stoumpos, C. C.; Evans, H. A.; Kontos, A. G.; Raptis, Y. S.; Falaras, P.; Van der Ven, A.; Kanatzidis, M. G.; Seshadri, R. Dynamic Stereochemical Activity of the Sn2+ Lone Pair in Perovskite CsSnBr3. *J. Am. Chem. Soc.* **2016**, *138* (36), 11820−11832.
(20) Gao, L.; Yadgarov, L.; Sharma, R.; Korobko, R.; McCall, K. M.; Fabini, D. H.; Stoumpos, C. C.; Kanatzidis, M. G.; Rappe, A. M.; Yaffe, O. Metal Cation s Lone-Pairs Increase Octahedral Tilting Instabilities in Halide Perovskites. *Mater. Adv.* **2021**, *2* (14), 4610−4616.
(21) Fabini, D. H.; Seshadri, R.; Kanatzidis, M. G. The Underappreciated Lone Pair in Halide Perovskites Underpins Their Unusual Properties. *MRS Bull.* **2020**, *45* (6), 467−477.
(22) Laurita, G.; Fabini, D. H.; Stoumpos, C. C.; Kanatzidis, M. G.; Seshadri, R. Chemical Tuning of Dynamic Cation Off-Centering in the Cubic Phases of Hybrid Tin and Lead Halide Perovskites. *Chem. Sci.* **2017**, *8* (8), 5628−5635.
(23) Chiara, R.; Morana, M.; Boiocchi, M.; Coduri, M.; Striccoli, M.; Fracassi, F.; Listorti, A.; Mahata, A.; Quadrelli, P.; Gaboardi, M.; Milanese, C.; Bindi, L.; Angelis, F. D.; Malavasi, L. Role of Spacer Cations and Structural Distortion in Two-Dimensional Germanium Halide Perovskites. *J. Mater. Chem. C* **2021**, *9* (31), 9899−9906.
(24) Di Girolamo, D.; Blundo, E.; Folpini, G.; Ponti, C.; Li, G.; Aldamasy, M. H.; Iqbal, Z.; Pascual, J.; Nasti, G.; Li, M.; Avolio, R.; Russina, O.; Latini, A.; Alharthi, F.; Felici, M.; Petrozza, A.; Polimeni, A.; Abate, A. Energy Distribution in Tin Halide Perovskite. *Sol. RRL* **2022**, *6* (8), No. 2100825.
(25) Hooper, R. W.; Ni, C.; Tkachuk, D. G.; He, Y.; Terskikh, V. V.; Veinot, J. G. C.; Michaelis, V. K. Exploring Structural Nuances in Germanium Halide Perovskites Using Solid-State 73Ge and 133Cs NMR Spectroscopy. *J. Phys. Chem. Lett.* **2022**, *13* (7), 1687−1696.
(26) Morana, M.; Wiktor, J.; Coduri, M.; Chiara, R.; Giacobbe, C.; Bright, E. L.; Ambrosio, F.; De Angelis, F.; Malavasi, L. Cubic or Not Cubic? Combined Experimental and Computational Investigation of the Short-Range Order of Tin Halide Perovskites. *J. Phys. Chem. Lett.* **2023**, *14* (8), 2178−2186.
(27) Corker, D. L.; Glazer, A. M.; Whatmore, R. W.; Stallard, A.; Fauth, F. A Neutron Diffraction Investigation into the Rhombohedral Phases of the Perovskite Series. *J. Phys.: Condens. Matter* **1998**, *10* (28), 6251−6269.
(28) Laurita, G.; Page, K.; Suzuki, S.; Seshadri, R. Average and Local Structure of the Pb-Free Ferroelectric Perovskites (Sr, Sn) TiO 3 and (Ba, Ca, Sn) TiO 3. *Phys. Rev. B* **2015**, *92* (21), No. 214109.
(29) Confalonieri, G.; Buscaglia, V.; Capitani, G.; Canu, G.; Rotiroti, N.; Bernasconi, A.; Pavese, A.; Dapiaggi, M. Local Distortion and Octahedral Tilting in BaCexTi1−xO3 Perovskite. *J. Appl. Crystallogr.* **2018**, *51* (5), 1283−1294.
(30) Octavio de Araujo, L.; Rêgo, C. R. C.; Wenzel, W.; Sabino, F. P.; Guedes-Sobrinho, D. Impact of the Polymorphism and Relativistic Effects on the Electronic Properties of Inorganic Metal Halide Perovskites. *J. Phys. Chem. C* **2022**, *126* (4), 2131−2140.
(31) Page, K.; Siewenie, J. E.; Quadrelli, P.; Malavasi, L. Short-Range Order of Methylammonium and Persistence of Distortion at the Local Scale in MAPbBr3 Hybrid Perovskite. *Angew. Chem.* **2016**, *128* (46), 14532−14536.
(32) Bernasconi, A.; Malavasi, L. Direct Evidence of Permanent Octahedra Distortion in MAPbBr3 Hybrid Perovskite. *ACS Energy Lett.* **2017**, *2* (4), 863−868.
(33) Bernasconi, A.; Page, K.; Dai, Z.; Tan, L. Z.; Rappe, A. M.; Malavasi, L. Ubiquitous Short-Range Distortion of Hybrid Perovskites and Hydrogen-Bonding Role: The MAPbCl3 Case. *J. Phys. Chem. C* **2018**, *122* (49), 28265−28272.
(34) Baskurt, M.; Wiktor, J. Exploring the Polaron Landscape in Germanium Halide Perovskites: $CsGeCl_3$, $CsGeBr_3$, and $CsGeI_3$. *J. Phys. Chem. Lett.* **2025**, *17*, 1569−1575.
(35) Fang, Y.; Wei, H.; Dong, Q.; Huang, J. Quantification of Re-Absorption and Re-Emission Processes to Determine Photon Recycling Efficiency in Perovskite Single Crystals. *Nat. Commun.* **2017**, *8* (1), 14417.
(36) Tang, Y.; Lesage, A.; Schall, P. $CsPbI_3$ Nanocrystal Films: Towards Higher Stability and Efficiency. *J. Mater. Chem. C* **2020**, *8* (48), 17139−17156.
(37) Schmidt, T.; Lischka, K.; Zulehner, W. Excitation-Power Dependence of the near-Band-Edge Photoluminescence of Semiconductors. *Phys. Rev. B* **1992**, *45* (16), 8989−8994.
(38) Smith, M. D.; Karunadasa, H. I. White-Light Emission from Layered Halide Perovskites. *Acc. Chem. Res.* **2018**, *51* (3), 619−627.
(39) Cho, C.; Palatnik, A.; Sudzius, M.; Grodofzig, R.; Nehm, F.; Leo, K. Controlling and Optimizing Amplified Spontaneous Emission in Perovskites. *ACS Appl. Mater. Interfaces* **2020**, *12* (31), 35242−35249.

https://doi.org/10.1021/acs.chemmater.6c00408
Chem. Mater. 2026, 38, 6446−6455

(40) Lei, L.; Dong, Q.; Gundogdu, K.; So, F. Metal Halide Perovskites for Laser Applications. *Adv. Funct. Mater.* **2021**, *31* (16), 2010144.
(41) Kieffer, J.; Valls, V.; Blanc, N.; Hennig, C. New Tools for Calibrating Diffraction Setups. *J. Synchrotron Rad* **2020**, *27* (2), 558−566.
(42) Juhás, P.; Davis, T.; Farrow, C. L.; Billinge, S. J. L. PDFgetX3: A Rapid and Highly Automatable Program for Processing Powder Diffraction Data into Total Scattering Pair Distribution Functions. *J. Appl. Crystallogr.* **2013**, *46* (2), 560−566.
(43) Farrow, C. L.; Juhas, P.; Liu, J. W.; Bryndin, D.; Božin, E. S.; Bloch, J.; Proffen, T.; Billinge, S. J. L. PDFfit2 and PDFgui: Computer Programs for Studying Nanostructure in Crystals. *J. Phys.: Condens. Matter* **2007**, *19* (33), 335219.
(44) Campbell, B. J.; Stokes, H. T.; Tanner, D. E.; Hatch, D. M. ISODISPLACE: A Web-Based Tool for Exploring Structural Distortions. *J. Appl. Crystallogr.* **2006**, *39* (4), 607−614.
(45) Stokes, H. T.; Hatch, D. M.; Campbell, B. J. *ISODISTORT, ISOTROPY Software Suite*. iso.byu.edu.
(46) Kühne, T. D.; Iannuzzi, M.; Del Ben, M.; Rybkin, V. V.; Seewald, P.; Stein, F.; Laino, T.; Khaliullin, R. Z.; Schütt, O.; Schiffmann, F.; Golze, D.; Wilhelm, J.; Chulkov, S.; Bani-Hashemian, M. H.; Weber, V.; Borštnik, U.; Taillefumier, M.; Jakobovits, A. S.; Lazzaro, A.; Pabst, H.; Müller, T.; Schade, R.; Guidon, M.; Andermatt, S.; Holmberg, N.; Schenter, G. K.; Hehn, A.; Bussy, A.; Belleflamme, F.; Tabacchi, G.; Glöß, A.; Lass, M.; Bethune, I.; Mundy, C. J.; Plessl, C.; Watkins, M.; VandeVondele, J.; Krack, M.; Hutter, J. CP2K: An Electronic Structure and Molecular Dynamics Software Package - Quickstep: Efficient and Accurate Electronic Structure Calculations. *J. Chem. Phys.* **2020**, *152* (19), 194103.
(47) VandeVondele, J.; Krack, M.; Mohamed, F.; Parrinello, M.; Chassaing, T.; Hutter, J. Quickstep: Fast and Accurate Density Functional Calculations Using a Mixed Gaussian and Plane Waves Approach. *Comput. Phys. Commun.* **2005**, *167* (2), 103−128.
(48) Bischoff, T.; Wiktor, J.; Chen, W.; Pasquarello, A. Nonempirical Hybrid Functionals for Band Gaps of Inorganic Metal-Halide Perovskites. *Phys. Rev. Materials* **2019**, *3* (12), No. 123802.
(49) Kresse, G.; Furthmüller, J. Efficient Iterative Schemes for *Ab Initio* Total-Energy Calculations Using a Plane-Wave Basis Set. *Phys. Rev. B* **1996**, *54* (16), 11169−11186.
(50) Kresse, G.; Hafner, J. *Ab Initio* Molecular Dynamics for Liquid Metals. *Phys. Rev. B* **1993**, *47* (1), 558−561.

https://doi.org/10.1021/acs.chemmater.6c00408
Chem. Mater. 2026, 38, 6446−6455